Scientia Iranica A (2023) 30(3), 902–917

Sharif University of Technology
Scientia Iranica
Transactions A: Civil Engineering
http://scientiairanica.sharif.edu

Simulation of the vaiont landslide via multi-body material point method with cohesive frictional interfaces

O.R. Barani[a] and H. Bagherzadeh*

Department of Civil Engineering, K. N. Toosi University of Technology, Tehran, Iran.

Received 4 October 2021; received in revised form 6 March 2022; accepted 21 November 2022

KEYWORDS
The Vaiont landslide;
Material point method;
Multi-body interaction;
Cohesive-frictional contact methodology;
deformable boundaries.

Abstract. In this study, the Vaiont landslide is simulated using an enhanced Material Point Method (MPM) capable of modeling multi-body interactions with cohesive-frictional interfaces. The interface model accuracy is examined through four elastic benchmarks. Afterward, the capability of the MPM is demonstrated in the simulation of two large deformation failures. After the verification phase, the Vaiont landslide is modeled considering three distinct elastoplastic bodies with cohesive-frictional interfaces. The calculated final configuration has excellent agreement with field observations. The effect of the number of masses contributing to the problem is investigated for the next step. Finally, the Vaiont landslide is modeled with rigid boundaries and a main sliding body. It is shown that the rigid boundary assumption may cause significant errors in the final geometry of the problem.

1. Introduction

The Vaiont landslide occurred in the reservoir of the Vaiont dam located in the Italian Alps (1963). Nearly, 250 million cubic meters of rock and soil became unstable and slid into the dam reservoir at a high velocity of approximately 30 meters per second. The landslide caused flood (tall waves up to 70 m above the dam crest) and ravaged the town of Longarone and nearby villages, resulting in more than 2000 causalities [1–6]. The Vaiont landslide is a reactivation of an old landslide [1]. The slope slid on top of a strong limestone formation filled with clay layers covering the failure surface. It is believed that the combined effects of intense rainfall and the rising of the reservoir level are the primary triggers of the failure [1,6,7]. High pore pressures at the reservoir level were encountered near the failure surface before the landslide [1]. The difference between limestone and clay permeabilities might cause high pore pressures in the vicinity of the clay layer [1]. The Vaiont landslide has been modeled via several numerical tools like the discrete element method, discontinuous deformation analysis, and meshless methods [5,6,8–11]. In the literature, the Vaiont landslide is initially considered a single mass on a rigid surface in a single-phase medium [5,6,8]. The modeling of the landslide provides better results when a thick clay layer is placed above the rigid boundary [10–14]. The Vaiont landslide is also simulated as a two- or even three-phase (solid, fluid, and heat) problem with embedded hydro-mechanical shear bands (or rock bridges) accounting for the complex geometry [15]. In this paper, the Vaiont landslide is simulated using the Material Point Method (MPM), a

*. *Corresponding author. Tel.: +98 21 88779475*
Fax: +98 21 88779476;
E-mail addresses: barani@kntu.ac.ir (O.R. Barani);
h.bagherzadeh@email.kntu.ac.ir (H. Bagherzadeh)

doi: 10.24200/sci.2022.59181.6098

powerful numerical tool to model extreme deformation problems with the following innovations: cohesive-frictional interfaces, degradation of friction-cohesion bonds, deformable boundaries, and multi-body interactions in three different cases.

First, the landslide is modeled using three contacting masses with deformable boundaries and cohesive-frictional interfaces. The Vaiont valley configuration and particle discretization were obtained from [12]. Then, to investigate the effect of the number of contacting bodies on the result, the Vaiont slide is discretized into five masses with cohesive-frictional interfaces and deformable boundaries. The bodies are selected using main faults and rock bridges provided by Alonso et al. [14–16]. The third case is devoted to simulating the landslide with the rigid boundary to highlight the deformable boundary role in the results. While the MPM can solve two- or three-phase problems [16–19], it is not computationally affordable to apply the main innovations of this paper in a two-phase framework due to the massive size of the problem. Therefore, all computations of this study are carried out under single-phase MPM simulation.

The remaining parts of this paper are presented as follows: Section 2 presents the formulations of the MPM and the multi-body contact methodology. Section 3 simulates six benchmarks to show the contact model accuracy and the capability of the numerical tool. Section 4 describes the Vaiont landslide characterization. Section 5 presents the simulation results of the Vaiont landslide. The effects of contacting masses, as well as rigid boundaries, are discussed in this section. Finally, Section 6 concludes this paper.

2. Formulation

2.1. Continuum mechanics

In continuum, the kinematic of a medium is presented using "initial" (X) and "current" (x) position (or coordinate) formulation. The link between the initial and current positions is presented using the deformation map (ϕ) as follows:

$$x_i = \phi_i(X_i, t). \tag{1}$$

The gradient of the deformation map (F) defines how the material is deformed locally as:

$$F_{ij} = \frac{\partial \phi_i}{\partial X_j}. \tag{2}$$

The deformation gradient Jacobian (J) interprets the condition of the medium after deformation. $J < 1$ implies that the volume is reduced, while $J > 1$ means the opposite [20]. Another terminology used in the continuum is the description of mesh as Lagrangian and Eulerian meshes. In the Eulerian formulation, the mesh is fixed in space while the Lagrangian mesh deforms as the solution continues (like FEM).

The governing equations of interest are conservation of mass and conservation of momentum. The total and updated Lagrangian formulations are two approaches to formulating the governing equations. The total Lagrangian uses the current coordination ($x_i = \phi_i(X_i, t)$), and the updated Lagrangian formulation uses the initial coordination system ($X = \phi^{-1}(x, t)$). Moreover, the Cauchy stress tensor (σ) is used in the updated Lagrangian, and the nominal stress (P) is used in the total Lagrangian formulation [21]. Let $v(X, t) = \delta x(X, 0)/\delta t$ be the velocity field defined over the initial coordinate (X); then, the total Lagrangian formulation of the governing equations is:

$$\rho(X, t)J(X, t) = \rho(X, 0), \tag{3}$$

$$\nabla^X P + \rho(X, t)b = \rho(X, t)\frac{\partial v}{\partial t}, \tag{4}$$

where $\rho(X, t)$ is the material density, $J(X, t)$ is the determinant of deformation gradient (F), b is the body force, and P is the nominal stress tensor [21]. The position and velocity are presented in the updated Lagrangian formulation with the current coordinate system as $v(x, t) = \frac{\delta X(x,0)}{\delta t}, X = \phi^{-1}(x, t)$, therefore, the conversation of linear momentum takes the following form:

$$\rho(x, t)\frac{\partial v(x, t)}{\partial t} = \nabla^x.\sigma(x, t) + \rho(x, t)b, \tag{5}$$

where $\sigma(x, t)$ is the Cauchy stress tensor. Because there is no mass source in the medium [21], we have:

$$\rho(x, t) = \rho(X, t). \tag{6}$$

The principle of virtual power is the collection of the weak form of the momentum equation, traction boundary conditions, and interior traction continuity, which is used for updated Lagrangian formulation. The test functions $\delta v_i(X, t)$ and the velocity trial functions $v_i(X, t)$ are used to develop the weak form of governing equation from the strong from as follows:

$$\int_\Omega \frac{\partial(\delta v_i)}{\partial x_j}\sigma_{ji}d\Omega - \int_\Omega \delta v_i \rho b_i d\Omega - \int_{\Gamma_{\bar{\tau}_i}} \delta v_i \bar{\tau}_i d\Gamma + \int_\Omega \delta v_i \rho \dot{v}_i d\Omega = 0. \tag{7}$$

The test and velocity functions are required to meet the following conditions [21]:

$$\delta v(X) \in u_0$$

$$u_0 = \{\delta v(X) | \, \delta v \in C^0(X), \delta v = 0_{on}\Gamma_v\}, \tag{8}$$

$$v(X,t) \in u$$

$$u = \{v(X,t) | \, v \in C^0(X), v = \bar{v}_{on}\Gamma_v\}, \tag{9}$$

where $C^0(X)$ is the smoothness or continuity of a function, and a function has C^n continuity if its nth derivative is a continuous function. The initial and boundary conditions are defined as follows:

$$v(X,0) = v(X), \tag{10}$$

$$x(X,t) = x(X), \tag{11}$$

$$v(X,t)|_{\Gamma_v} = \bar{v}(X,t), \tag{12}$$

$$r|_{\Gamma_r} = \bar{r} = \sigma_{ji} n_j, \tag{13}$$

where Γ_v is the prescribed velocity boundary; r and Γ_r are the traction and prescribed traction boundary; and n is the unit normal to the domain surface [21].

2.2. Material Point Method (MPM)

The MPM is a robust numerical method to simulate large deformations of history-dependent materials [22–24]. The most important feature of MPM is its mixed Eulerian-Lagrangian solution scheme [22]. MPM consists of a background Eulerian grid (grid) and sets of Lagrangian particles (Figure 1(a)). Bodies are divided into sub-segments (regions), and the physical and mechanical properties of these sub-segments are concentrated into the material points called particles (Figure 1(a)). The grid in the MPM provides a framework to process data and integrate the governing equation [25,26]. There are three phases of calculation in each time step. At phase one, particle data such as mass, momentum, and velocity are mapped to the grid nodes utilizing shape functions. At phase two, the weak form of governing equations is solved at grid nodes producing the nodal result fields (Figure 1(b)). At phase three, the nodal results update the particle position and velocity (Figure 1(c)). At the end of each time step, the grid returns to the initial geometry (Figure 1(d)).

In this section, the notation of the paper is presented. In the MPM formulation, there are three types of variables (Eulerian, Lagrangian, and mixed). Eulerian variables are defined at grid nodes and have a life span of one computational cycle, like nodal momentum, velocity, and mass. Eulerian variables are presented with a subscript uppercase index (e.g., v_{Ii}). Lagrangian variables are defined in particles specifically and are preserved through computation duration like mass, velocity, stress tensor, and strain tensor. Lagrangian variables are presented using the p superscript (M^p for mass and v_i^p for the velocity of particle p). Mixed variables are defined at grid nodes for a particular particle. For example, shape functions and their derivatives are defined at grid nodes based on the particle position. Mixed variables are presented using a subscript index for nodes and superscript for particles (e.g., N_I^p).

The major components of the weak form (mass matrix, internal force vector, and external force vector) in the updated Lagrangian MPM are:

$$M_I = \sum_{p=1}^{n_p} N_I^p m^p, \tag{14}$$

$$v_{Ii} = \sum_{p=1}^{n_p} N_I^p v_i^p, \tag{15}$$

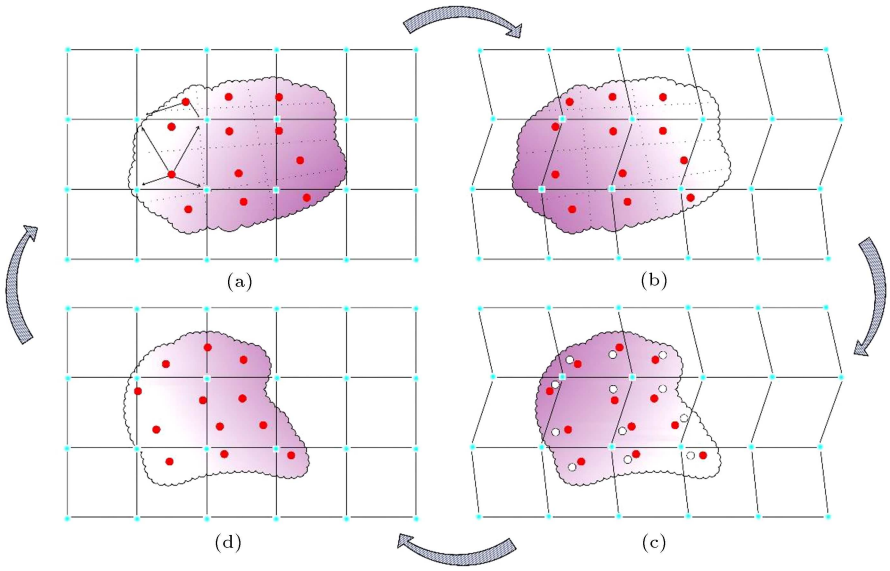

Figure 1. Four cycles of the material point method computation: (a) MP mapping to nodes, (b) nodal solution field, (c) mapping back from nodes to MP, and (d) discarding old grid and generating new one.

$$p_{Ii} = \sum_{p=1}^{n_p} N_I^p v_i^p m^p, \tag{16}$$

$$f_{Ii}^{\text{int}} = -\sum_{p=1}^{n_p} \frac{\partial N_I^p}{\partial x_j} \sigma_{ji}^p \frac{m^p}{\rho^p}, \tag{17}$$

$$f_{Ii}{}^{ext} = \sum_{p=1}^{n_p} N_I^p b_i^p m^p, \tag{18}$$

where M_I is the grid mass matrix, $f_{Ii}{}^{\text{int}}$ and $f_{Ii}{}^{ext}$ are internal and external force vectors, M_I is the nodal mass matrix, n_p represents the total number of particles, N_I^p is the shape function value of particle (p) at node I, and m^p is the mass of the material point p. Also, v_i^p is the particle (p) velocity vector, v_{Ii} is the velocity vector of node I, p_{Ii} is the momentum vector of the node I, σ_{ji}^p is the particle p stress tensor, ρ^p is the density of material point p, and b_i^p is the particle p body force.

The nodal acceleration field is integrated explicitly (phase two). It is customary to use explicit integration because implementing implicit time integration for rapid movement problems yields no significant advantage in the MPM [27,28]. In explicit time integration, the acceleration, velocity, and displacement fields are calculated as:

$$a_{Ii}^{(t+\Delta t)} = (f_{Ii}^{ext(t)} + f_{Ii}^{int(t))}/M_I, \tag{19}$$

$$v_{Ii}{}^{(t+\Delta t)} = v_{Ii}{}^{(t)} + a_{Ii}{}^{(t+\Delta t)}\Delta t, \tag{20}$$

$$u_{Ii}{}^{(t+\Delta t)} = u_{Ii}{}^{(t)} + v_{Ii}{}^{(t+\Delta t)}\Delta t. \tag{21}$$

The position, velocity, and stress tensor of material points are updated from mapping back the nodal result field to particles as:

$$v_i{}^{p(t+\Delta t)} = v_i{}^{p(t)} + \sum_{I=1}^{I_n} N_I^p v_{Ii}^{(t+\Delta t)}, \tag{22}$$

$$x_i^{p(t+\Delta t)} = x_i^{p(t)} + \sum_{I=1}^{I_n} N_I^p u_{Ii}^{(t+\Delta t)}, \tag{23}$$

where $x_i^{p(t+\Delta t)}$ and $v_i^{p(t+\Delta t)}$ are updated position and velocity vector of material point p, I_n is the number of the element nodes (containing), $v_{Ii}^{(t+\Delta t)}$ is the velocity vector of node I, and $u_{Ii}^{(t+\Delta t)}$ is the displacement field of node I.

The stress tensor of material points is integrated from the Jaumann rate of the stress tensor. The rates of deformation tensor (D) and the spin tensor (W) are extracted from the nodal velocity field as [21]:

$$L^p{}_{ij} = \frac{\partial v_i^p}{\partial x_j}, \tag{24}$$

$$D^p{}_{ij} = \frac{1}{2}(L^p{}_{ij} + (L^p{}_{ij})^T), \tag{25}$$

$$W^p{}_{ij} = \frac{1}{2}(L^p{}_{ij} - (L^p{}_{ij})^T), \tag{26}$$

where $L^p{}_{ij}$ is the velocity derivation, D^p is the rate of deformation tensor, and W^p is the spin tensor of the material point (p). From spin and rate of deformation tensors, the rate of Cauchy stress tensor is determined and integrated to update the stress tensor of particles for the next time step:

$$\dot{\sigma}_{ij}^p = \frac{\partial \sigma_{ij}^p}{\partial t} = C_{ijkl}^{\sigma_j} : D_{kl}^p - W_{ik}^p \sigma_{kj}^p - \sigma_{ik}^p (W^T)_{kj}, \tag{27}$$

$$\sigma^{p(t+\Delta t)} = \sigma^{p(t)} + \dot{\sigma}^p \Delta t, \tag{28}$$

where $C_{ijkl}^{\sigma_j}$ is the Jaumann elastoplastic constitution matrix, and $\sigma^{p(t+\Delta t)}$ is the updated stress tensor of particle p. The effects of the rigid rotation on the Cauchy stress tensor of a particle are corrected with the Jaumann rate of the stress tensor. For example, when a stressed bar rotates at 90 degrees, the components of the stress tensor vary from $(\sigma_x = \sigma_0, \sigma_y = 0)$ to $(\sigma_x = 0, \sigma_y = \sigma_0)$. The stress evolved as $\dot{\sigma} = C^{ep} : D$, which is not valid in the case of 90 degrees rotation because the rate of deformation tensor is zero and the stress tensor remains constant [19]. Additional terms in Eq. (27) are used to eradicate the adverse effects of large rotations or translations effects on the stress tensor [21].

2.3. Frictional contact force

The contact procedure is introduced in MPM via the multi-velocity field algorithm [29]. The multi-velocity field generates one background grid for each body and detects contact nodes, contact force, and contact direction based on the difference in the velocity field. After mapping each body to a specified grid, a global search is performed at all grid nodes to determine the contact nodes. A contact node (I) is defined as:

$$(v_{Ii}^{b_1} - v_{Ii}^{b_2}) n_{Ii}^{b_1} > 0, \tag{29}$$

where $v_{Ii}^{b_1}$ is the velocity of body b_1 at grid node I and $n_{Ii}^{b_1}$ is the contact normal as:

$$n_{Ii}^{b_i} = \sum_{p=1}^{n_p} N_{I,i}^{p,b_i} m^{p,b_i} \Bigg/ \left| \sum_{p=1}^{n_p} N_{I,i}^{p,b_i} m^{p,b_i} \right|, \tag{30}$$

where $N_{I,i}^{p,b}$ is the particle p (form body b) shape function derivation at node I and, m^{p,b_i} is the mass of the particle P of the body b_i.

The contact force is obtained by modifying the nodal momentum of each body. First, the free momentum $p_{Ii}^{\prime b_i(t+\Delta t)}$ for each body is calculated as follows:

$$p_{Ii}^{\prime b_i(t+\Delta t)} = p_{Ii}^{b_i(t)} + (f_{Ii}^{int,b_i} + f_{Ii}^{ext,b_i})\Delta t, \tag{31}$$

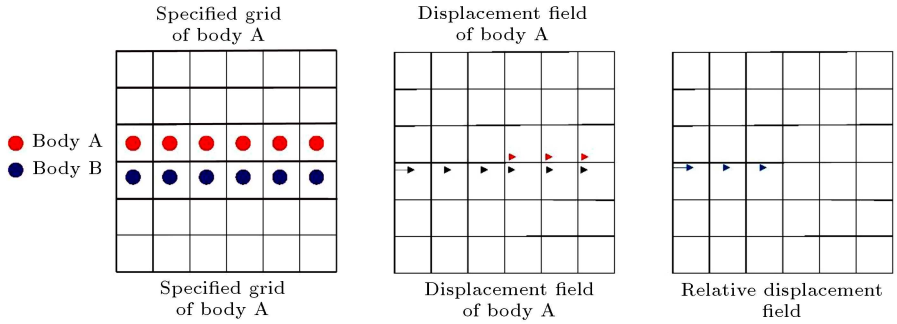

Figure 2. Obtaining relative displacement in an interface.

where $p_{Ii}^{b_i(t)}$ is the momentum vector of the body b_i; $f_{Ii}^{\int,b_i}$ and f_{Ii}^{ext,b_i} are internal and external forces of the body b_i at node I. At all contact nodes, the momentum field must satisfy the impenetrability condition or:

$$(m_I^{b_1} p_{Ii}^{b_2} - m_I^{b_2} p_{Ii}^{b_1}) n_{Ii}^{b_2} = 0, \tag{32}$$

where $m_I^{b_i}$ is the mass of body b_i at node I, $p_{Ii}^{b_2}$ is the body b_i momentum at node I, and $n_{Ii}^{b_2}$ is the contact normal of body b_2 at node I. Based on the impenetrability condition, the total contact force (f^c) of contacting bodies is:

$$f_{Ii}^c = [(m_I^{b_1} p'^{b_2}_{Ii}{}^{(t+\Delta t)} - m_I^{b_2} p'^{b_1}_{Ii}{}^{(t+\Delta t)})/ \Delta t(m_I^{b_1} + m_I^{b_2})]. \tag{33}$$

The normal (f_{Ii}^{cnf}) and tangential (f_{Ii}^{ctf}) contact forces are formulated as:

$$f_{Ii}^{cnf} = [(m_I^{b_1} p'^{b_2}_{Ii}{}^{(t+\Delta t)} - m_I^{b_2} p'^{b_1}_{Ii}{}^{(t+\Delta t)})/ \Delta t(m_I^{b_1} + m_I^{b_2})] n_{Ii}^{b_2}, \tag{34}$$

$$f_{Ii}^{ctf} = [(m_I^{b_1} p'^{b_2}_{Ii}{}^{(t+\Delta t)} - m_I^{b_2} p'^{b_1}_{Ii}{}^{(t+\Delta t)})/ \Delta t(m_I^{b_1} + m_I^{b_2})] [t_{Ii}^{b_2}, \tag{35}$$

where the contact tangent vector $t_{Ii}^{b_1}$ is presented as follows [30]:

$$t_{Ii}^{b_2} = \frac{(v_{Ii}^{b_2} - v_{Ii}^{b_1}) - (v_{Ij}^{b_2} - v_{Ij}^{b_1}) n_{Ij}^{b_2} n_{Ii}^{b_2}}{\left| (v_{Ii}^{b_1} - v_{Ii}^{b_2}) - (v_{Ij}^{b_1} - v_{Ij}^{b_2}) n_{Ij}^{b_2} n_{Ii}^{b_2} \right|}. \tag{36}$$

2.4. Cohesive contact force

The cohesion force between two contacting bodies mobilizes in small displacement and perishes in large relative displacement due to degradation. This paper proposes a new technique to consider the degradation of cohesive contact force via the MPM. The degradation force is evaluated via relative nodal displacement of two contacting bodies. Particles in the vicinity of an interface (interface particles) represent the surface of contact and the contact area. The cohesive resisting force of interface particles on the (specified) grid is:

$$f_{Ii}^{cf} = \sum_{p=1}^{n_p} N_I^p c^p A_i^p, \tag{37}$$

where f_{Ii}^{cf} is the cohesive resisting force at grid node I, c^p is the cohesion parameter, and A_i^p is the cross-section (e.g., interface area) of the particle p which is aligned with the direction of the motion. The cohesion parameter needs modification based on the relative displacement of two contacting bodies or:

$$c^p = f\left(\sum N_I^P u_I^r\right), \tag{38}$$

where N_I^P is the shape function of the particle p at node I, and u_I^r is the relative displacement between two contacting bodies at node I (A and B in Figure 2) as:

$$u_I^r = \left|u_I^A\right| - \left|u_I^B\right|. \tag{39}$$

The relative displacement u_I^r is then mapped back to all interface particles to change the value of the cohesion parameter (considering the degradation effect).

2.5. Computational plasticity

A detailed formulation of plasticity is out of the scope of this study, and only essential parts of plasticity used in this paper are addressed here. Plastic deformation happens when the stress state of the material passes the following condition (yield surface) [31]:

$$f(\sigma) = k, \tag{40}$$

where f is an arbitrary function of stress and k is the experimentally plastic threshold. The plastic strain increment $d\varepsilon_{ij}^p$ is proportional to the stress gradient of the plastic potential function Q as [31]:

$$d\varepsilon_{ij}^p = d\lambda \frac{\partial Q}{\partial \sigma_{ij}}, \tag{41}$$

where $d\lambda$ is a proportionality constant (plastic multiplier).

Table 1. Physical properties of benchmarks.

Benchmark	Dim (m)	Density (kg/m^3)	Friction coefficient	Poisson's ratio	Inclination angle
1	1.6	2000	Vary	0.3	$\pi/3, \pi/4$
2	1	2000	Vary	0.3	$\pi/6$
3	0.1	2000	0.1	0.3	$\pi/6$

For earth materials (soil, rock, or concrete), the Drucker-Prager and Mohr-Coulomb yield criteria are suitable because they contain the first invariant of the stress tensor. D–P and M–C yield criteria take the following forms [21,31]:

$$f(\sigma) = \alpha J_1 + \sqrt{J'_2} = \kappa, \tag{42}$$

$$\tau = c - \sigma_n \tan\varphi, \tag{43}$$

where $J_1 = \sigma_{ii}$ is the first invariant of stress tensor, $J'_2 = 0.5\sigma'_{ij}\sigma'_{ij}$ is the second invariant of the deviatoric stress tensor, α, κ are Drucker-Prager, and c, φ are Mohr-Coulomb model constants (material parameters). Conventional geotechnical experiments produce the Mohr-Coulomb parameters. For obtaining Drucker-Prager parameters from Mohr-Coulomb constants, yield surface coincidence between the two mentioned models is necessary. The inner coincidence of Mohr-Coulomb and Drucker-Prager yield surfaces results in the following equivalencies [31]:

$$\alpha = \frac{2\sin\varphi}{\sqrt{3}(3+\sin\varphi)},$$

$$\kappa = \frac{6c\sin\varphi}{\sqrt{3}(3+\sin\varphi)}. \tag{44}$$

After yielding, the deformation of a material is both elastic and plastic. During stress increment, the strain increment $d\varepsilon_{ij}$ is divided between the elastic and plastic strain increment $d\varepsilon^p_{ij}$ as:

$$d\varepsilon_{ij} = d\varepsilon^e_{ij} + d\varepsilon^p_{ij}. \tag{45}$$

By implementing the elastic strain-stress relation and flow rule in Eq. (40), the general form of the elasto-plastic stress-strain relation is obtained as:

$$d\varepsilon_{ij} = \frac{d\sigma'_{ij}}{2\mu} + \frac{(1-2\nu)}{E}\delta_{ij}d\sigma_{kk} + d\lambda\frac{\partial Q}{\partial\sigma_{ij}}. \tag{46}$$

To evaluate collective plastic strain on each particle or to devise a rule for updating plastic threshold (κ) in computational plasticity, the equivalent plastic strain is used which takes the following form:

$$d\bar{\varepsilon}^p = \sqrt{(\frac{2}{3})d\varepsilon^p_{ij}d\varepsilon^p_{ij}}. \tag{47}$$

The increment of equivalent plastic strain is added to the total equivalent plastic strain, which is used further for hardening computations.

3. Benchmarks

The proposed contact technique is validated via six benchmarks. Four elastic dynamic contact problems (rolling sphere, sliding blocks, and failure initiation) are modeled, and two large deformation failure problems with elasto-plastic behavior. Properties of elastic problems are presented in Table 1. All the problems are simulated using the explicit form of the MPM.

3.1. The rolling sphere

The movement of a rolling sphere on an inclined frictional plane, with an available closed-form solution, is the first dynamic benchmark [32]. The closed-form solution is presented for the center of mass displacement alongside the plane axes in two conditions [30]:

$$x = x_0 + \frac{1}{2}gt^2(\sin\theta - \mu\cos\theta),$$

$$\tan\theta > 3\mu \qquad \text{(Roll and slip)}, \tag{48.a}$$

$$x = x_0 + \frac{5}{14}gt^2(\sin\theta),$$

$$\tan\theta \leq 3\mu \qquad \text{(Roll)}. \tag{48.b}$$

To ensure that the two sliding cases are considered here, two different inclination angles with two different friction coefficients are employed (Table 2). Figure 3 shows the numerical results for the sphere center of mass displacement alongside the plane axis compared to the closed-form solution. As shown in Figure 3, MPM simulates this problem accurately.

3.2. The sliding block on a plane

In this section, the sliding of a block on an inclined frictional plane is considered a benchmark problem

Table 2. The dynamic condition of the rolling sphere for four trials.

Inclination angle	Friction coefficient	Rolling condition
$\pi/3$	0.2	Slip
$\pi/3$	0.6	Pure rolling
$\pi/4$	0.1	Slip
$\pi/4$	0.4	Pure rolling

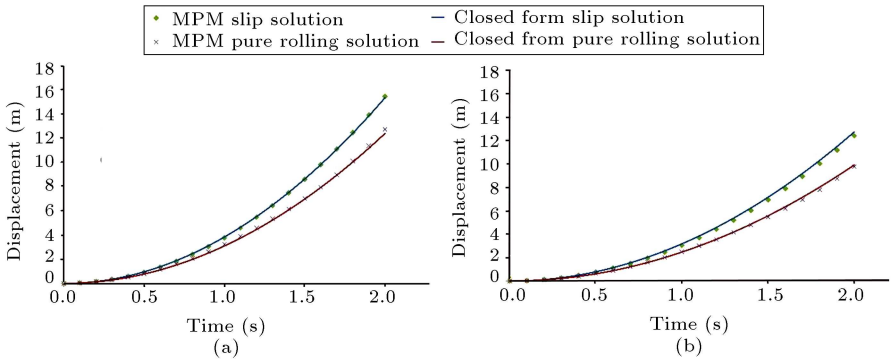

Figure 3. The rolling sphere benchmark: (a) displacement diagram for $\theta = \pi/4$ and (b) displacement diagram for $\theta = \pi/3$.

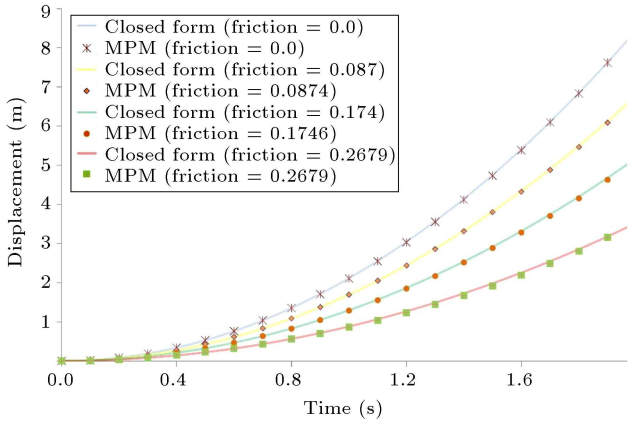

Figure 4. The sliding block benchmark; closed-form solution versus the material point method simulation.

Table 3. The computational error for the sliding block benchmark.

Friction coefficient	$t = 0.5$ s	$t = 1$ s	$t = 1.5$ s	$t = 2$ s
0	0.138%	0.383%	0.472%	0.118%
0.087	0.812%	0.778%	0.380%	0.63%
0.174	0.278%	0.772%	1.060%	1.020%
0.267	1.660%	1.870%	1.650%	1.653%

with a larger contact area. This benchmark is also carried out by 3D-DDA and 2D-DDA numerical methods successfully [33–38]. The exact solution in the case of slip condition is as Eq. (48.a). The displacement of the block alongside the plane axis and the closed-form solutions are presented in Figure 4. Table 3 presents the simulation error for each friction coefficient.

3.3. The sliding block on a cohesive-frictional plane

The second benchmark is simulated again with the frictional-cohesive inclined plane with constant cohesion (100 Pa). Figure 5(a) shows the total value of the cohesive and frictional forces from the MPM modeling and the closed-form solution. Figure 5(b) shows the agreement between the MPM simulation and the exact solution for the block displacement alongside the plane axis.

3.4. The failure initiation

A column consisting of two blocks on an inclined frictional plane is considered stimulating the static and dynamic behaviors of bodies associated with sliding and toppling (Figure 6(a)). Zhang et al. (2016) [39] simulated this problem with the cohesive 3D-DDA numerical method. This problem is simulated using deformable blocks in the MPM. The physical properties of this system are presented in Table 4. The cohesion and Young's modulus values of the plane are carefully chosen to ensure that the lower block remains still and the plane stays undeformed after the impact [39]. Figure 6 presents the displacement of the upper block and the deformation of the upper block due to impact is visible (Figure 6(d)).

3.5. Slope failure under gravitational loading

The validation of constitutive equations with emphasis on the large deformation scheme is carried out via simulation of slope failure under gravity loading. This problem has been solved before via the MPM for cohesive and non-cohesive soils under various body

Table 4. Physical properties of column block system.

Part	Dimension (m)	Density (kg/m^3)	Young's modulus (MPa)	Cohesion value (Pa)	Friction coefficient	Poisson's ratio	Inclination angle
Upper block	0.5	2000	2.2	0	0.28	0.25	–
Lower block	1	2000	2.2	0	0.28	0.25	–
Interfaceplane	–	–	300	1000	0.9	0.25	$\pi/4$

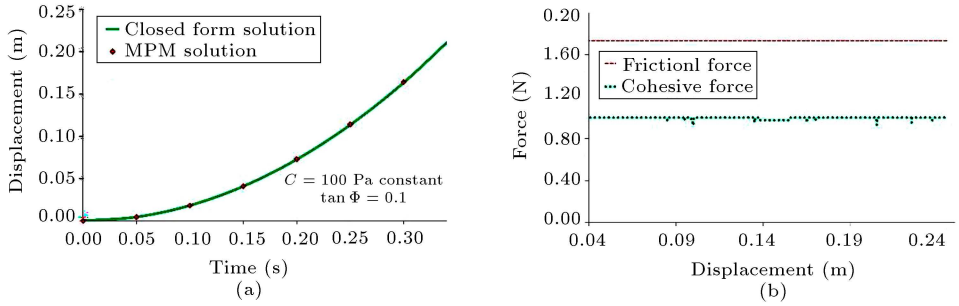

Figure 5. The cohesive-frictional sliding block diagrams: (a) Closed-form solution versus the material point method predictions and (b) Total cohesive and frictional force versus displacement.

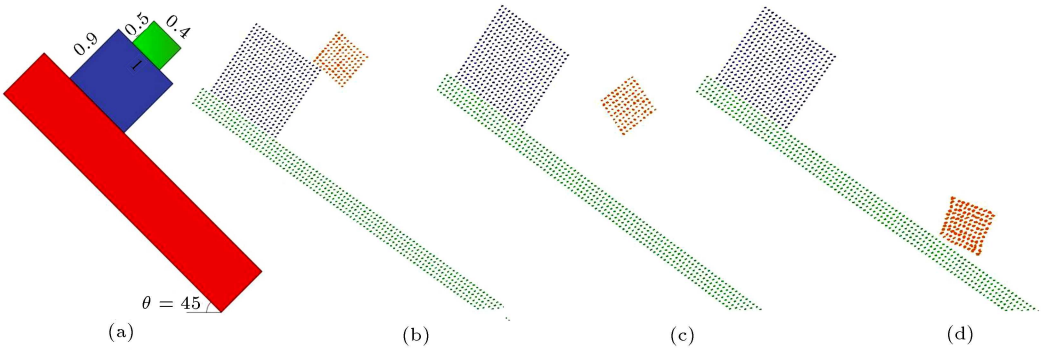

Figure 6. The failure initiation problem: (a) configurations, (b) position at $t = 0.31$ s, (c) position at $t = 0.74$ s, and (d) position at $t = 0.97$ s.

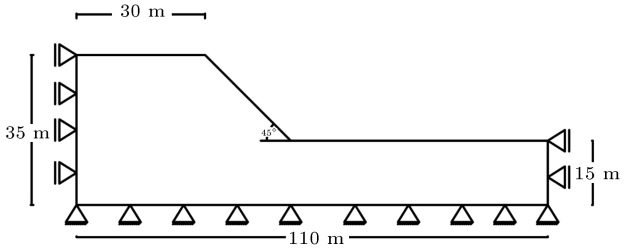

Figure 7. Configuration of the simple cohesive soil slope benchmark.

forces and material properties [40]. Here, only the case of cohesive soil under gravity loading is considered. The geometry of the slope alongside boundary conditions is presented in Figure 7. The cohesive soil has the following material properties: Young's modulus 70 MPa; friction angle 20 degrees; cohesion value 10 kPa (without the cohesion degradation); and the Poisson ratio 0.3. Non-associative plastic flow rule of Drucker-Prager with no dilatancy and tension strength of 27.48 kPa is considered for soil material [40].

The model configuration is as follows: Particle spacing is 0.5 m, background cell size is 1 m, and the domain is represented with 19640 material points. In Figure 8, the equivalent plastic strain and displacement of the slope from MPM modeling and another study [40] are presented. The agreement between plastic strain contours and general displacement of slop is visible, as shown in Figure 8.

3.6. Failure of a slope with non-cohesive material

Large deformation of non-cohesive slope failure is selected for the last benchmark. This experiment was carried out on a slope with artificial soil under a plane strain conditions in [41]. Aluminum bars of 1 to 1.5 mm diameter with 50 mm length and the density of 2650 kg/m^3 are employed to model soil particles. The block soil sample (200 × 100 × 50 mm) is formed from aluminum bars confined with two flat vertical walls. The collapse of the block is initiated by removing the right wall suddenly. Based on the shear box test results, the cohesion value and friction angle of the aluminum-bar assemblage are evaluated at 0 and 19.8, respectively [41]. A Poisson ratio of 0.3 and a bulk modulus of 0.7 MPa are recommended for the artificial soil [41]. This problem is solved with a particle spacing of 1.25 mm under gravity loading of 9.81 m/s^2. The Drucker-Prager constitutive model with the non-associative flow rule (zero dilation angle) is assumed, and parameters are approximated with the inner coincidence yield surfaces.

The simulated final equivalent plastic strain on the deformed shape of the block is presented in Figure 9. As shown in Figure 9, the results of the current study are in agreement with other numerical studies. In addition, the final experimental configuration is shown in Figure 9(d). A comparison between the current study and experimental results for failure line and sur-

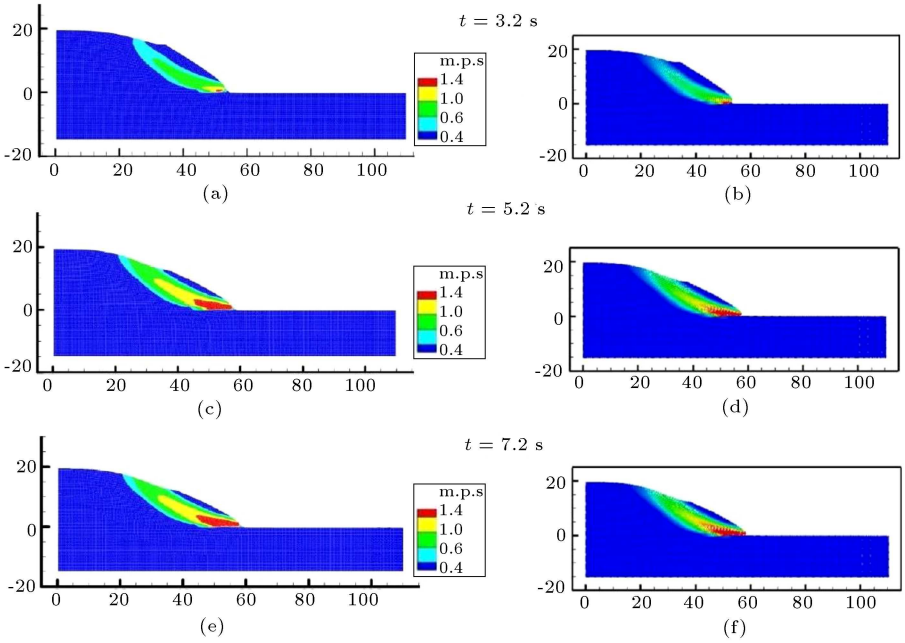

Figure 8. Effective plastic strain contours or evolution of the shear band; the material point method simulation for: (a) $t = 3.2$ s, (c) $t = 5.2$ s, (e) $t = 7.2$ s, Results obtained from Huang et al. [40] (2015) as: (b) $t = 3.2$ s, (d) $t = 5.2$ s, (f) $t = 7.2$ s.

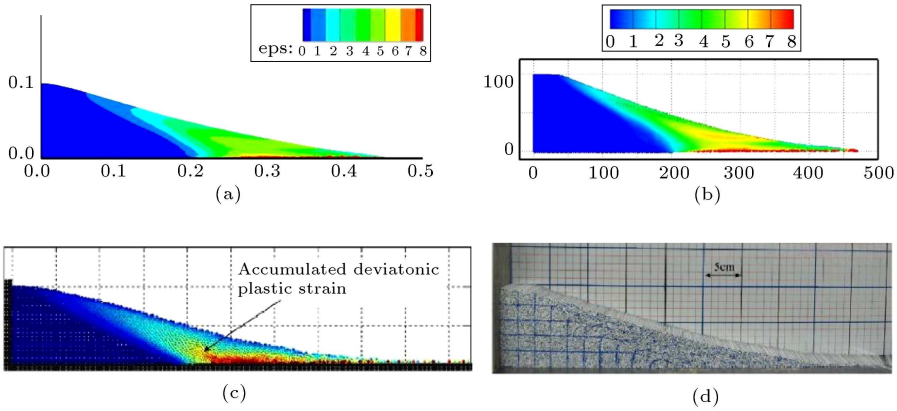

Figure 9. Effective plastic strain contours: (a) this study, (b) Huang et al. (2015) [40], (c) Bui et al. (2008) [41], the smoothed particle hydrodynamics simulation, and (d) final configuration of aluminum bars from the experiment [41].

face configuration is presented in Figure 10. Although there is agreement between the MPM simulation result and the experiment, the error in the computation result arises from the particle discretization and grid crossing error. Discretizing a medium into finer particles with finer mesh yields better results while imposing a severe cost on the computation effort. The grid crossing error is another cause of numerical oscillation and error in the MPM [42].

4. Characterization of vaiont landslide

The geological and geotechnical properties of the Vaiont landslide are described here. The failure surface of the landslide is crucial because it controls the volume of the sliding mass and, therefore, all kinematic behaviors. Several numerical modeling methods have investigated the failure surface configuration [43–45]. It is generally accepted that the landslide slid on a weak continuous thin, rich clay layer [10,12,45]. Although some researchers challenged this assumption [46,47], solid evidence from road tunnels and other field observations proved that the interface layer was continuous and contained 50–80% clay minerals [10,41,48–50].

Hendron and Patton (1987) [1] proposed an average friction angle of 12° for the clay layer based on experimental data. This value is widely accepted and consistent with laboratory test results and numerical investigations [4,43]. During the slide, this residual friction angle further degraded [1,43]. Ibanez and Haztor (2018) [43] showed that the degradation during rapid motion was about 25% of friction angle and

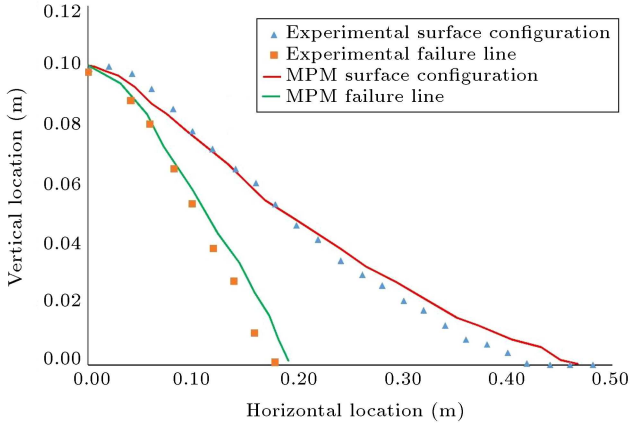

Figure 10. Final configuration and failure surface from the material point method simulation and experiment [41].

recommended a friction coefficient of 0.16 [1]. The friction coefficient of 0.16 was supported by rapid torsion tests of the clay material from the slide [3]. The maximum cohesion values of 50 kPa to 150 kPa were suggested for the clay layer [4,5,50].

5. Simulation of the vaiont slide

This study considers the clay layer as a frictional-cohesive interface between bodies. Due to the rapid movement, high-velocity test results are considered in the model via the linear degradation technique [43]. The initial and residual friction coefficient values are considered 0.2 and 0.16 [3,43]. The cohesion value of the clay layer also varies due to degradation. Because there is no degradation algorithm for the clay layer in the literature, a linear degradation curve for the cohesion value is assumed. Bilinear friction and cohesion degradation laws were adopted from [41] with the relative degradation displacement of one percent of particle spacing. Degradation curves of friction coefficient and cohesive value are presented in Figure 11.

The Vaiont landslide domain is often considered as the main sliding body that slides on a rigid base toward a rigid boundary [4,8,12,45]. In this study, the Vaiont valley, including the sliding mass and boundaries, is defined as distinct deformable masses with cohesive-frictional interfaces. First, three bodies are employed to model the landslide. Then, the effect of several interacting masses on the quality of results is investigated by modeling the problem as five deformable masses. Finally, the effect of rigid boundary conditions is investigated in a two-mass problem.

5.1. Triple bodies simulation

This section defines the Vaiont landslide as three contacting masses, as shown in Figure 12. The failure mechanism is defined as the movement of body A (main sliding elastoplastic mass) on body B (elastically deformable boundary mass) toward body C (elastoplastic weathered ancient deposit) [1,8]. Near one million material points in three structured background grids are used to represent the contacting bodies. In the preprocessing stage, marginal particles of each body are flagged as the interface layer (cohesion-friction or pure friction). Cohesion-friction interfaces are defined between bodies A-C and B-C initially, while the frictional interface is detected automatically based on the velocity field of each body (explained in Subsection 2.3). The number of material points for spatial discretization of contacting bodies is presented in Table 5.

Mechanical properties of the Vaiont valley rock masses for the model input were obtained from [4] and [51]. The friction angle, internal cohesion (Mohr-Coulomb model parameters), Young's modulus,

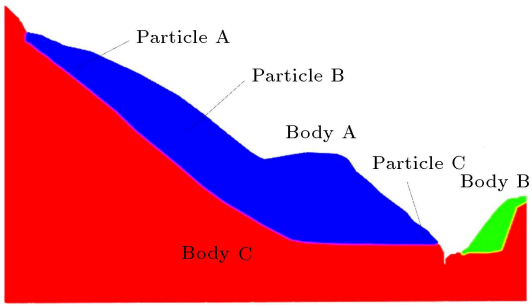

Figure 12. The Vaiont valley triple bodies representation.

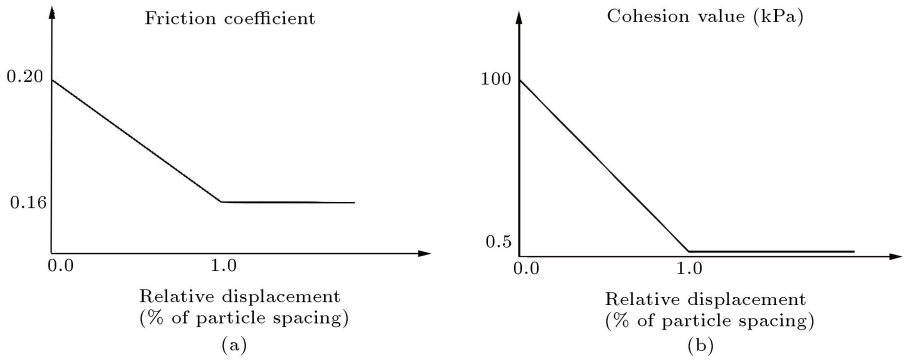

Figure 11. The linear degradation of mechanical properties of the clay layer: (a) Friction coefficient and (b) Cohesive value.

Table 5. The material point method definition of the Vaiont landslide.

Parameter	Spacing	Body A MP numbers	Body B MP numbers	Body C MP numbers	Time step
value	1 (m)	493148	83750	453518	1.20e–6 (s)*

* The time step value is based on recommendations in [18]. The total run-out duration is approximately three months.

Table 6. Material properties of Vaiont landslide bodies after the study of Wolter et al. (2013) [4].

Part	Density (kg/M^3)	Young's modulus (MPa)	Poisson's ratio	Internal friction angle	Internal cohesion
Body A	2000–2700	500	0.25	30–45	0.1 (MPa)
Body B	2100–2700	500	0.25	30–40	0.1 (MPa)
Body C	2700	500	0.25	45	0.1 (MPa)

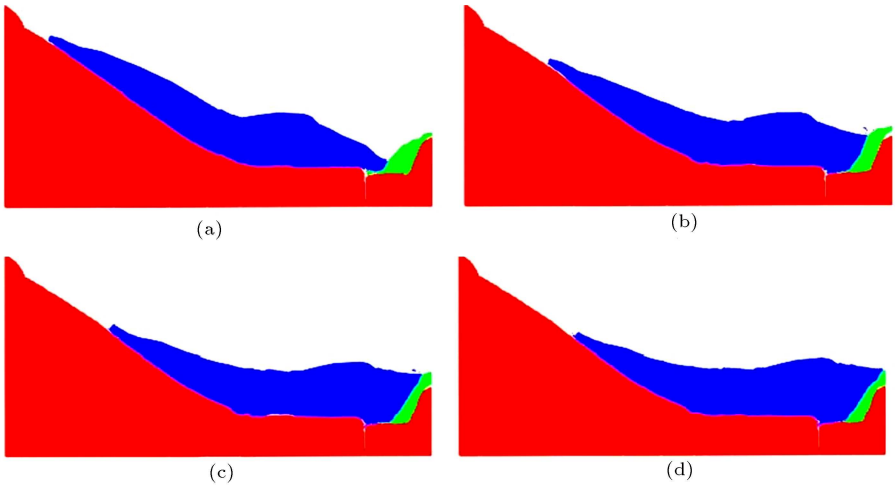

Figure 13. The landslide run-out configuration: (a) $t = 10$ s, (b) $t = 17.5$ s, (c) $t = 22.5$ s, and (d) $t = 33.5$ s.

and the Poisson ratio of rock masses used in this study are presented in Table 6. The Drucker-Prager yield surface with a tension cut-off of 0.6 MPa is used to model all masses in the landslide, and an inner coincidence approximation of Drucker-Prager with Mohr-Coulomb yield surfaces is used to obtain the material model parameters [4].

Figure 13 represents the configuration of the Vaiont valley from impact (8 s) to the stable condition (33.5 s). The final configuration of the Vaiont landslide from the MPM numerical modeling is presented in Figure 14 compared to the other numerical studies and field investigations [5,10,11]. As shown in Figure 14, the MPM result for the final configuration is in better agreement with field investigations. Given that the Vaiont landslide is a complex and large-scale problem, it is suitable to check if the calculated results meet previous investigations into the following issues:

- The landslide duration; based on previous studies, landslide duration is estimated to be between 17 s and 45 s [1,4,9,11,12,43]. In this study, the main sliding mass (body A in Figure 12) reached the stable condition after 33.5 s, which is an acceptable value;

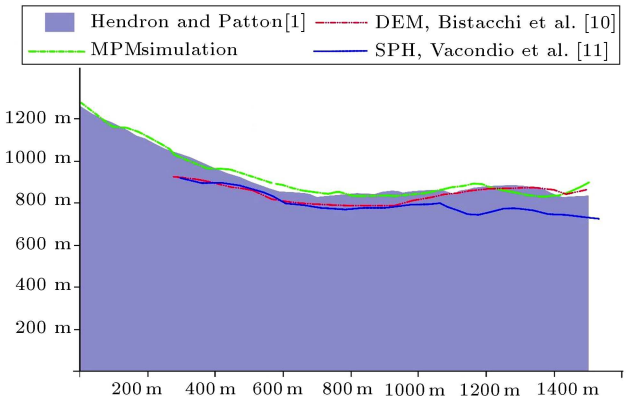

Figure 14. Final configuration of the Vaiont valley from field investigations and numerical simulations.

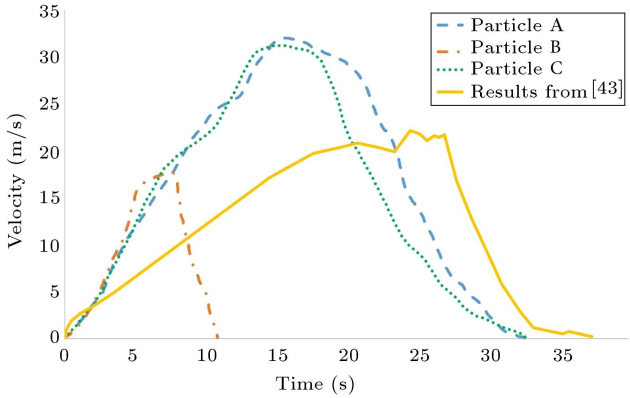

Figure 15. Time-velocity graphs of trial particles during slide.

- The peak velocity; from numerical simulations to empirical estimations, the peak velocity of the landslide is estimated between 25 m/s and 50 m/s [5,10,12,43]. The mean peak velocity of sliding mass in this study is predicted as 31.4 m/s, which is in good agreement with other investigations [43];
- The time-velocity curve of the landslide; the time-velocity curve of three trial particles (shown in Figure 12) is captured and presented in Figure 15. The DDR simulation time-velocity curve of the Vaiont landslide is presented in Figure 15 [43]. The shape of the time-velocity graph from DDR analysis (Figure 15) is like the time-velocity curve (particles A and B in Figure 15) obtained by the MPM analysis presented. It is noteworthy that particle C, which is near the failure surface, has a shorter movement duration as well as a lower peak velocity than other particles (Figure 15);
- The velocity-displacement curve of the main sliding body; Henderon and Patton (1987) [1] proposed analytical velocity-displacement curves of the landslide for various friction losses due to degradation. Figure 16 presents the velocity-displacement curve of particle A from the numerical simulation versus the analytical estimation [1,43]. As seen in Figure 16, the MPM landslide displacement is estimated at 556.47 m which is in good agreement with the analytical value of 500–600 m [1,43].

5.2. Five masses modeling

Five distinct bodies (considering main faults) are chosen to represent the Vaiont landslide, as shown in Figure 17 with following features [1,8]: body 1 defines the outer geometry of the valley. Bodies 2, 3, and 4 represent the main sliding part with cohesive-frictional interfaces. Body 5 represents the weathered saturated mass of the northern slope [1,8]. Material properties are considered the same as the triple-mass system in the previous section.

The result of the simulation is presented in Figure 18. Body 4 behaves as follows: after failure, it fills the deepest part of the valley and then, it becomes a frictional-cohesive base for body 3. The upper interface of body 4 undergoes shear displacement from the tangential component of contact force (from body 3). Also, body 4 experiences volumetric plastic deformation due to the normal component of the contact force that originated from the massive surcharge of bodies 2 and 3. After the main impact, the momentum causes body 2 to move from its original position on body 3. The run-out duration is 29 seconds with a peak velocity of 34 meters per second in this case. Figure 19 presents the final configuration of the valley in five and three masses systems. It can be stated that the effect of increasing distinct masses on the final configuration of the valley is negligible; however, it considerably increases computation efforts.

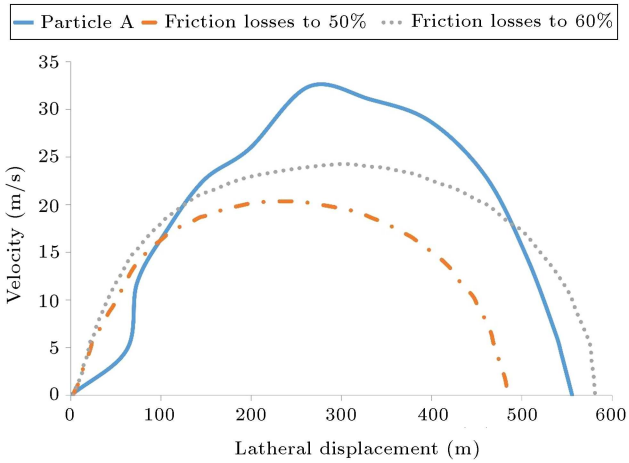

Figure 16. Comparison between the velocity-lateral displacement curve of the analytical modeling for various friction losses [1] and the material point method result.

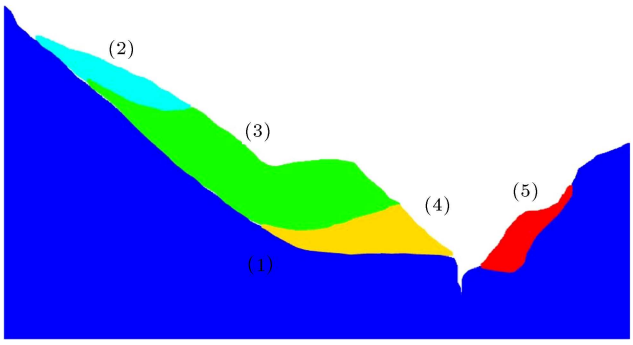

Figure 17. Initial configuration of the Vaiont valley for five interactional masses.

5.3. Effect of rigid boundary conditions

A simulation of the landslide with rigid boundary conditions is performed in this section to highlight the importance of defining deformable boundaries. Approximately 1.6 million particles define the landslide in two distinct bodies (Figure 20). An elasto-plastic

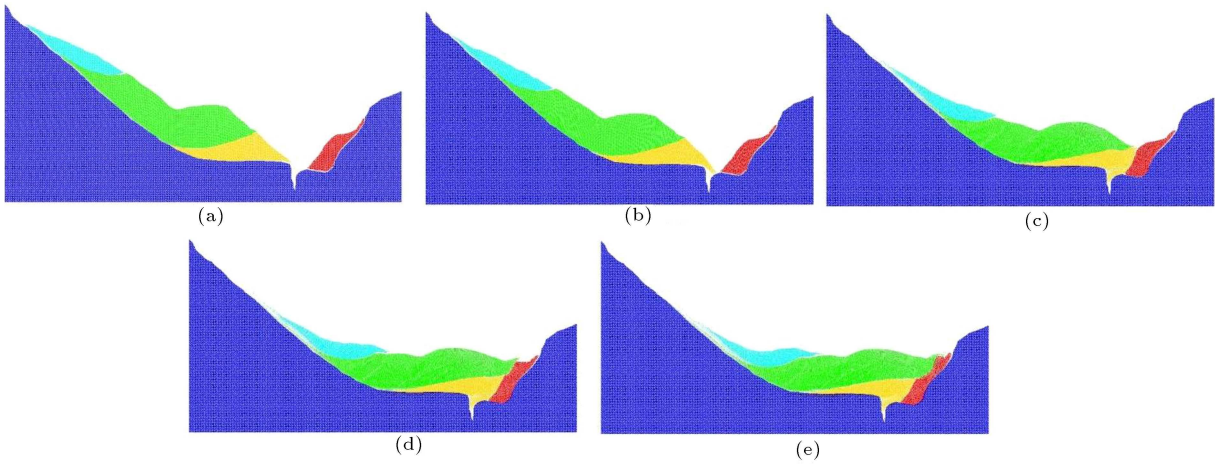

Figure 18. The landslide run-out configuration: (a) $t = 0$ s, (b) $t = 8$ s, (c) $t = 19$ s, (d) $t = 24$ s, and (e) $t = 29$ s.

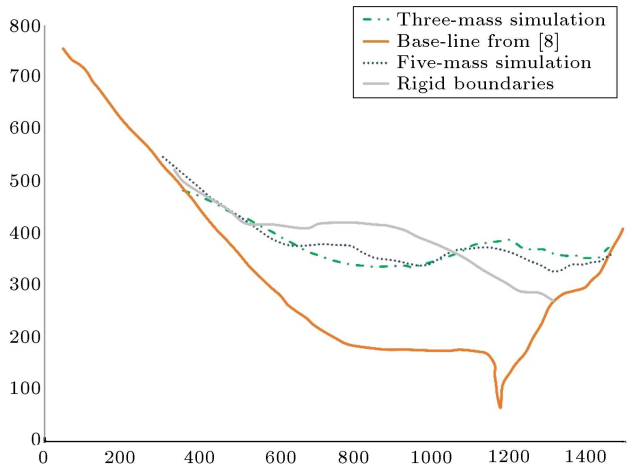

Figure 19. The effect of number of masses and rigid boundaries at final configuration of the Vaiont valley; Baseline obtained from [1,4].

material (Table 6) is used for the sliding mass, and a relatively stiff elastic material is used for the boundary. The results (Figure 19) show that the displacement is reduced using rigid boundaries. The landslide duration and peak velocity are obtained at 24 s and 19.9 m per second, respectively. These values are about 30% less than the corresponding values in the first case showing the importance of deformable boundaries in the numerical results, although these values are still in the acceptable range.

6. Conclusions and remarks

This paper implemented a cohesive-frictional contact methodology in the Material Point Method (MPM) to simulate large and rapid deformations. Six numerical large deformation benchmarks were simulated to validate the contact methodology and constitutive material laws. Afterward, the Vaiont landslide was modeled considering three different cases. First, the landslide was modeled using three contacting masses. In this case, the final configuration of the slide had good agreement with field investigations. The landslide duration was estimated to be 33.5 seconds, and the central sliding mass reached the maximum mean velocity of 31.4 m/s. In addition, the lateral displacement of the landslide was calculated as 556.47 m. All the mentioned parameters were in agreement with the results of previous studies.

To investigate the effect of the number of contacting bodies on results, five masses considering the main faults and beddings were selected as the second case. Although more realistic behavior from bodies was observed during failure, no significant improvement in the final configuration of the valley was encountered. The third case was devoted to simulating the landslide with rigid boundary conditions to highlight the role of deformable boundary conditions in the model. Results showed that the rigid boundaries caused significant error in the final configuration of the valley. In

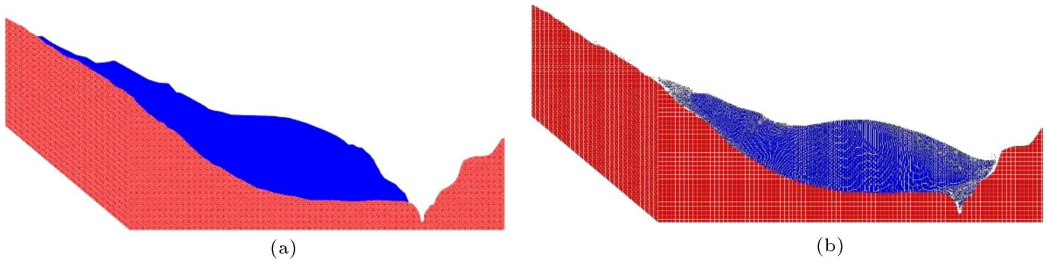

Figure 20. Initial (a) and final (b) configurations of the Vaiont valley considering rigid boundary conditions.

addition, it was shown that the error in landslide duration and peak velocity was about 30%.

References

1. Hendron, A.J. and Patton, F.D. "The Vaiont slide-a geotechnical analysis based on new geologic observation of the failure surface", *Engineering Geology*, **24**, pp. 475–491 (1987).
2. Evans, S.G., Mugnozza, A.L., Strom, A.L., et al. "Landslides from massive rock slope failure and associated phenomena", Springer, Dordrecht (2006).
3. Ferri, F., Toro, GD., Hirose, T., et al. "Low to high velocity frictional properties of the clay rich gouges from the slipping zone of the 1963 Vaiont slide (northern Italy)", *Journal of Geophysical Research*, **116**, pp. 1–17 (2011).
4. Wolter, A., Havaej, M., Zorzi, L., et al. "Exploration of the kinematics of the 1963 Vajont slide, Italy, using a numerical modelling toolbox", *Italian Journal of Engineering Geology and Environment*, **6**, pp. 599–612 (2013).
5. Boon, C.W., Houlsby, G.T., and Utili, S. "New insights in the 1963 Vajont slide using 2D and 3D Distinct Element Method analyses", *Géotechnique*, **64**(10), pp. 800–816 (2014).
6. Zhao, T., Utili, S., and Crosta, G.B. "Rockslide and impulse wave modelling in the vajont reservoir", *Rock Mechanics and Rock Engineering*, **49**, pp. 2437–2456 (2016). https://doi.org/10.1007/s00603-015-0731-0
7. Zaniboni, F. and Tinti, S. "Numerical simulations of the 1963 Vajont landslide, Italy: application of 1D Lagrangian modelling", *Natural Hazards*, **70**, pp. 567–592 (2017). https://doi.org/10.1007/s11069-013-0828-2
8. Sitar, N., MacLaughlin, M.M., and Doolin, D.M. "Influence of kinematics on landslide mobility", *Journal of Geotechnical and Geoenvironmental*, **131**, pp. 715–728 (2005). DOI: https://doi.org/10.1061/(ASCE)1090-0241(2005)131:6(716)
9. Ward, D. and Day, S. "The 1963 landslide and flood at Vaiont reservoir Italy A tsunami ball simulation", *Italian Journal of Geosciences*, **130**(1), pp. 16–26 (2011).
10. Bistacchi, A., Massironi, M., Superchi, L., et al. "3D geological model of the 1963 Vajont landslide", *Italian Journal of Engineering Geology and Environment*, **6**, pp. 531–539 (2013). https://doi.org/10.4408/IJEGE.2013-06.B-51
11. Vacondio, R., Mignosa, P., and Pagani, S. "3D SPH numerical simulation of the wave generated by The Vaiont rockslide", *Advances in Water Resources*, **59**, pp. 146–156 (2013). https://doi.org/10.1016/j.advwatres.2013.06.009
12. Liano-serna, M.A., Farias, M.M., and Perdroso, D.M. "An assessment of the material point method for modelling large scale run-out processes in landslides", *Landslides*, **13**, pp. 1057–1066 (2016). https://doi.org/10.1007/s10346-015-0664-4
13. Yerro, A., Pinyol, N.M., and Alonso, E.E. "Internal progressive failure in deep-seated landslides", *Rock Mechanics and Rock Engineering*, **49**, pp. 2317–2332 (2016). https://doi.org/10.1007/s00603-015-0888-6
14. Alonso, E.E. "Triggering and motion of landslides", *Géotechnique*, **71**, pp. 3–59 (2020). https://doi.org/10.1680/jgeot.20.RL.001
15. Alonso, E.E., Yerro, A., and Pinyol N.M. "Recent developments of the Material Point Method for the simulation of landslides", *International Symposium on Geohazards and Geomechanics: Earth and Environmental Science* (2015). https://doi.org/10.1088/1755-1315/26/1/012003
16. Pinyol, N.M., Alvardo, M., Alonso, E.E., et al. "Thermal effects in landslide mobility. Géotechnique", **68**(6), pp. 528–545 (2018). http://dx.doi.org/10.1680/jgeot.17.P.054
17. Kularathna, S., Liang W., Zhao T., et al. "A semi-implicit material point method based on fractional-step method for saturated soil", *International Journal for Numerical and Analytical Methods in Geomechanics*, **45**(10), pp. 1–32 (2021). https://doi.org/10.1002/nag.3207
18. Zheng, X., Pisanó, F., Vardon, P.J., et al. "An explicit stabilized material point method for coupled hydromechanical problems in two-phase porous media", *Computers and Geotechnics*, **135** (2021). https://doi.org/10.1016/j.compgeo.2021.104112
19. Sun, Z., Liu, K., Wang, J., et al. "Hydro-mechanical coupled b-spline material point method for large deformation simulation of saturated soils", *Engineering Analysis with Boundary Elements*, **133**, pp. 330–340 (2021). https://doi.org/10.1016/j.enganabound.2021.09.023
20. Gonzalez, O. and Stuart, A. "A first course in continuum mechanics", Cambridge University Press (2008).
21. Belytschko, T., Liu, W.K., Moran, B., et al., *Nonlinear Finite Element for Continua and Structures*, John Wiley and Sons Ltd (2014).
22. Sulsky, D., Chen, Z., and Schreyer, H.L. "A particle method for history-dependent materials", *Computer Modeling in Engineering and Sciences*, **118**, pp. 179–196 (1994). https://doi.org/10.1016/0045-7825(94)90112-0
23. Sulsky, D., Chen, Z., and Schreyer, H.L. "Application of a particle-in-cell method to solid mechanics", *Computer Physics Communications*, **87**, pp. 236–252 (1995). https://doi.org/10.1016/0010-4655(94)00170-7
24. Sulsky, D. and Schreyer, H.L. "Axisymmetric form of the material point method with applications to upsetting and Taylor impact problems", *Computer Modeling in Engineering and Sciences*, **139**, pp. 409–429 (1996). https://doi.org/10.1016/S0045-7825(96)01091-2

25. Zhang, X., Sze, K.Y., and Ma, S. "An explicit material point finite element method for hyper-velocity impact", *International Journal for Numerical Methods in Engineering*, **66**, pp. 689–706 (2006). https://doi.org/10.1002/nme.1579

26. Zhang, X., Chen, Z., and Liu, Y., *The Material Point Method a Continuum-Based Particle Method for Extreme Loading Cases*, Academic Press Publications (2016).

27. Chen, Z.P., Qiu, X.M., Zhang, X., et al. "Improved coupling of finite element method with material point method based on a particle-to-surface contact algorithm", *Computer Methods in Applied Mechanics and Engineering*, **293**, pp. 1–19 (2015). https://doi.org/10.1016/j.cma.2015.04.005

28. Chen, Z., Zhang, X., Qiu, X., et al. "A frictional contact algorithm for implicit material point method", *Computer Methods in Applied Mechanics and Engineering*, **321**(1), pp. 124–144 (2017). https://doi.org/10.1016/j.cma.2017.04.006

29. Bardenhagen, S.G., Guilkey, J.E., Roessig, K.M., et al. "An improved contact algorithm for the material point method and application to stress propagation in granular material", *Computer Methods in Applied Mechanics and Engineering*, **2**(4), pp. 509–522 (2010). https://doi.org/10.3970/cmes.2001.002.509

30. Lian, Y.P., Zang, X., and Liu, Y. "Coupling of finite element method with material point method by local multi-mesh contact method", *Computer Methods in Applied Mechanics and Engineering*, **200**, pp. 3482–3494 (2011). https://doi.org/10.1016/j.cma.2011.07.014

31. Owen, D.R.J. and Hinton, E., *Finite Element in Plasticity*, Theory and Practice, Pineridge Press Limited (1980).

32. Ma, Z.T., Zhang, X., and Huang, P. "An object-oriented MPM framework for simulation of large deformation and contact of numerous grains", *Computer Modeling in Engineering and Sciences*, **55**, pp. 61–87 (2010).

33. Beyabanaki, S.A.R., Ferdosi, B., and Mohammadi, S. "Validation of dynamic block displacement analysis and modification of edge-to-edge contact constraints in 3-D DDA", *International Journal of Rock Mechanics and Mining Sciences*, **46**(7), pp. 1223–1234 (2009). https://doi.org/10.1016/j.ijrmms.2008.12.001

34. Wang, B., Vardon, P.J., Hicks, M.A., et al. "Development of an implicit material point method for geotechnical applications", *Computers and Geotechnics*, **71**, pp. 159–167 (2016). https://doi.org/10.1016/j.compgeo.2015.08.008

35. Zhang, Y., Xu, Q., Chen, G., et al. "Extension of discontinuous deformation analysis and application in cohesive-frictional slope analysis", *International Journal of Rock Mechanics and Mining Sciences*, **70**, pp. 533–545 (2014). https://doi.org/10.1016/j.ijrmms.2014.06.005

36. Biran, G.Y. and Hatzor, Y.H. "Benchmarking the numerical Discontinuous Deformation Analysis method", *Computers and Geotechnics*, **71**, pp. 30–46 (2016). https://doi.org/10.1016/j.compgeo.2015.08.003

37. Ma, S., Zhao, Z., Nie, W., et al. "Implementation of displacement-dependent Barton-Bandis rock joint model into discontinuous deformation analysis", *Computers and Geotechnics*, **86**, pp. 1–8 (2017). https://doi.org/10.1016/j.compgeo.2016.12.030

38. Zhang, H., Liu, S., Zheng, L., et al. "Extensions of edge-to-edge contact model in three-dimensional discontinuous deformation analysis for friction analysis", *Computers and Geotechnics*, **71**, pp. 261–275 (2016). https://doi.org/10.1016/j.compgeo.2015.09.010.

39. Zhang, H., Liu, S., Chen, G., et al. "Extension of three-dimensional discontinuous deformation analysis", *International Journal of Rock Mechanics and Mining Sciences*, **86**, pp. 65–79 (2016). https://doi.org/10.1016/j.ijrmms.2016.03.021

40. Huang, P., Li, S., Guo, H., et al. "Large deformation failure analysis of the soil slope based on the material point method", *Computers and Geosciences*, **4**, pp. 1–13 (2015). https://doi.org/10.1007/s10596-015-9512-9

41. Bui, H.H., Fukagawa, R., Sako, K., et al. "Lagrangian meshfree particles method (SPH) for large deformation and failure flows of geomaterial using elastic-plastic soil constitutive model", *International Journal for Numerical and Analytical Methods in Geomechanics*, **32**, pp. 1537–1570 (2008). https://doi.org/10.1002/nag.688

42. Steffen, M., Kirby, M.K., and Berzins, M. "Decoupling and balancing of space and time errors in the material point method (MPM)", *International Journal of Rock Mechanics and Mining Sciences*, **82**(10), pp. 1207–1243 (2010). https://doi.org/10.1002/nme.2787

43. Ibanez, J.P. and Haztor, Y.H. "Rapid sliding and friction degration: lessons from the catastrophic Vajont landslide", *Engineering Geology*, **244**, pp. 96–106 (2018). https://doi.org/10.1016/j.enggeo.2018.07.029

44. Broili, L. "New knowledges on the geomorphology of the Vaiont slide slip surface", *Rock Mechanics and Engineering Geology*, **5**, pp. 38–88 (1967).

45. Pinyol, N.M., Alvardo, M., and Alonso, E.E. "Thermal effects in landslide mobility", *Géotechnique*, **65**, pp. 528–545 (2018). https://doi.org/ 10.1680/jgeot.17.P.054

46. Müller, L. "New consideration on the Vaiont slide", *Rock Mechanics and Engineering Geology*, **6**, pp. 1–91 (1968).

47. Bernoulli, D. and Peters, T. "Traces of rhyolitis-trachitic volcanism in the upper Jurassic of the South-

ern alps", *Eclogae Geologicae Helvetiae*, **63**, pp. 609–621 (1970).

48. Bromhead, E.N. "Reflections on the residual strength of clay soils, with special reference to bedding-controlled landslides", *Quarterly Journal of Engineering Geology and Hydrogeology*, **46**(2), pp. 132–155 (2013). https://doi.org/10.1144/qjegh2012-078

49. Müller-Salzburg, L. "The vajont catastrophe-a personal review", *Engineering Geology*, **24**, pp. 423–444 (1987).

50. Alonso, E.E. and Pinyol, M.N. "Criteria for rapid sliding I. A review of Vaiont case", *Engineering Geology*, **114**(3), pp. 198–210 (2010). https://doi.org/10.1016/j.enggeo.2010.04.018

51. Ghirotti, M. "Aspetti geomeccanici e modellazione numerica della frana del Vajont", Phd thesis, universityá di Parma, Ferrara, Firenze e Pavia, Italy (1992).

Biographies

Omid Reza Barani is an Assistant Professor at the Civil Engineering Department at K. N. Toosi University of Technology, Tehran, Iran. He holds a BSc degree from Sharif University of Technology (1999), and MSc degree from Isfahan University of Technology (2002), and a PhD from Sharif University of Technology (2011). His research interests include numerical methods in engineering, computational geomechanics, fracture mechanics, and petroleum geomechanics.

Hossein Bagherzadeh is a PhD at the Civil Engineering Department at K. N. Toosi University of Technology, Tehran, Iran. He holds a BSc degree from Babol University of Technology (2012) and MSc degree from Sharif University of Technology (2014). His research interests include numerical methods in engineering, computational geomechanics, and experimental research in rock joints.